Supplement of Nat. Hazards Earth Syst. Sci., 21, 941–960, 2021
https://doi.org/10.5194/nhess-21-941-2021-supplement

Natural Hazards and Earth System Sciences
Open Access
EGU

Supplement of

Attribution of the Australian bushfire risk to anthropogenic climate change

Geert Jan van Oldenborgh et al.

Correspondence to: Geert Jan van Oldenborgh (oldenborgh@knmi.nl)

Supplementary material

This supplementary material contains two attributions of the most important factors underlying the extremely high fire weather (FWI) index in Australia in 2019/20: extreme heat (section S1) and extreme drought (section S2) at the annual and monthly timescales. In contrast to the corresponding variables in the FWI, the observational analysis of which is limited to the reanalysis period (i.e., the recent few decades) and the climate model analysis to just a few models due to data availability, we here make use of larger climate model ensembles over longer time periods. In the heat extremes section, we find that some observational datasets do not reproduce the station data and that climate models have problems reproducing the resulting observed characteristics of heat extremes within the uncertainties of the century-long analysis, which are smaller than for the shorter reanalysis period of the FWI in the main text. The drought analysis reveals that the trend observed over the reanalysis period is not representative of the longer term trends in the fire season or annual mean drought. These conclusions are used to make the attribution statements of the main text more accurate.

S1 Extreme heat

S1.1 The heat of 2019/20

Australia started 2019 during an extreme summer that was the country's hottest on record in terms of both seasonal mean temperatures and the seasonal mean of daily maximum temperatures. This record summer occurred, at least in part, in Australia's warmest and driest year on record and directly after the current hottest summer on record (2018/2019 was 1.52 °C above the seasonal average). Overall, Australia has warmed by 1 °C since 1910, however, most of this warming has occurred since 1950. The frequency of extreme heat events in Australia outnumber extreme cool events by 12:1 (Lewis and King, 2015), and the frequency of heatwaves have also increased since 1950 (Perkins and Alexander, 2013). Increasing trends in heatwave intensity, frequency and duration are projected throughout the 21st Century (Cowan et al., 2014), with a clear link between global warming and overall heatwave changes (Perkins-Kirkpatrick and Gibson, 2017).

S1.2 Temporal Event Definition

For this analysis, we choose an event definition that represents the impacts of extreme heat on the fire risk: the annual (July-June, in order to ensure a continuous summer season) maximum of a 7-day moving average of daily maximum temperatures, TX7x. With this we aim to answer the question of whether and by how much the probability of a 7-day average maximum temperature at least as high as observed in the study region in 2019 has changed as a result of anthropogenic climate change. Note that standard definitions of heat waves as recommended by the Expert Team on Climate Change Detection and Indices (ETCCDI) do not correspond well with the risk of bushfires and are therefore less suitable for this analysis.

S1.3 Observational temperature data and methods

We use a number of datasets developed using independent methodologies to assess observed daily maximum temperatures, as the number of stations in the area varies greatly through time (Fig. S1) and hence the method chosen to interpolate between them is important before about 1970. Note that our trend definition, changes proportional to the Global Mean Surface Temperature (GMST), gives most weight to the period after 1975, when global mean temperatures started to increase strongly due to anthropogenic emissions.

The first dataset we consider is the Berkeley Earth climate analysis (Rohde et al., 2013), a gridded dataset derived statistically from available station data. Although maximum daily temperature data is available from 1880 onwards, here we only use data from 1910 onwards, since the use of Stevenson huts was only standardized throughout Australia from this time onwards and earlier measurements are likely biased high by several degrees (Trewin, 2013). Berkeley Earth uses large spatial decorrelations lengths in their interpolation method that are more appropriate for annual rather than daily data. The next dataset is the Australian Water Availability Project (AWAP) analysis 1910–now, which is constructed by imposing anomalies from station data on a high-resolution climatology. This is augmented by a simple average of a set of quality-controlled Australian Climate Observations Reference Network – Surface Air Temperature (ACORN-SAT) stations (Trewin, 2013). These include a

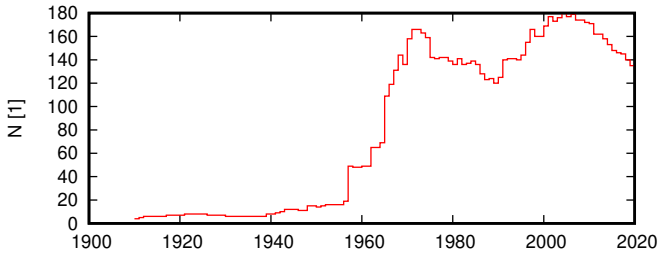

Figure S1. Number of Global Historical Climatology Network-Daily (GHCN-D, Menne et al., 2016) daily maximum temperature stations with at least 10 years of data in the study area.

large number of coastal stations. The ACORN-SAT daily gridded analysed fields were not yet available at the time of writing. Note that we cannot use monthly datasets like HadCRUT4 or Climate Research Unit Time Series (CRU TS) for an analysis of weekly maximum temperatures.

We also considered two types of reanalysis data. (1) Long-term reanalyses that are constrained only or mainly by Sea Surface Temperature (SST) and sea-level pressure (SLP): the NOAA Twentieth Century Reanalysis version 3 (20CRv3 Slivinski et al., 2019), the European Centre for Medium-Range Weather Forecasts (ECMWF) Coupled ReAnalysis of the Twentieth Century 1900-2010 (CERA-20C Laloyaux et al., 2018), which assimilates SST, wind and salinity and temperature profiles, and the older ERA-20C reanalysis, which assimilates sea-level pressure and marine winds but uses the UK Met Office Hadley centre HadISST 2.1.0.0 analysis and Coupled Model Intercomparison Project Phase 5 (CMIP5) radiative forcings as boundary conditions. (2) Shorter reanalyses that assimilate as much data as possible, including satellite observations: the Japanese Reanalysis (JRA-55 Kobayashi et al., 2015), a reanalysis product from the Japan Meteorological Agency (JMA) using 4D Variational data assimilation in their TL319 global spectral model spanning 1958–2019 at the time of writing. Finally we also included the much shorter fifth generation ECMWF atmospheric reanalysis (ERA5, Hersbach et al., 2019) 1979–now as that is used in the attribution of the Fire Weather Index.

A comparison of the observational analyses and reanalyses reveals some striking differences (Fig. S2). The long-term trend in the Berkeley Earth analysis is larger than in the AWAP analysis, but individual extreme years appear suppressed compared to AWAP, most notably in 1938/39. This is relevant for the attribution analysis as these extreme years define the probability distribution of high extremes. We investigated this particular event on 8–14 January 1939 in more detail. The ACORN-SAT station data confirms its existence. It also coincided with large bushfires, including the 'Black Friday' fires on 13 January 1939. In addition to long-term trend and correlation, we thus use the 1939 event as another guiding proxy to decide whether to include a particular temperature dataset or not. Even though the Berkeley Earth reanalysis is well-correlated with the AWAP analysis in general ($r = 0.86 \pm 0.06$ since 1910, $r = 0.96 \pm 0.02$ since 1960), this figure shows that we cannot trust the distribution of the high extremes.

We next consider the long-term reanalyses that do not assimilate land near-surface temperatures. The 1939 event does appear in the 20CRv3 reanalysis, which apparently captures the extraordinary circulation that led to the very high temperatures

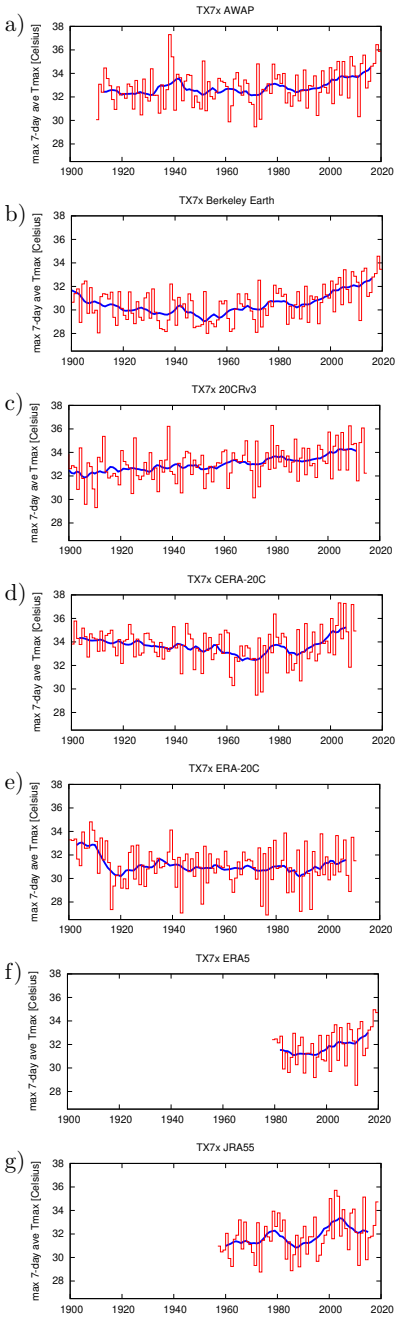

Figure S2. The highest 7-day running mean of daily maximum temperature of the July–June year in a) the AWAP analysis, b) Berkeley Earth, c) 20CRv3 reanalysis, d) CERA-20C ensemble mean (DJF maximum), e) ERA-20C ensemble mean (DJF maximum), f) ERA5 and g) JRA-55. The purple line indicates a 10-yr running mean. The value for 2020 is based on the observations up to January, which captures the highest value.

in southeastern Australia that week well enough to generate very high near-surface temperatures associated with it. Over the whole century, the correlation of TX7x with AWAP is $r = 0.79 \pm 0.10$ since 1910, $r = 0.90 \pm 0.06$ since 1960, which implies it captures the interannual variability reasonably well. We do not use the data before 1900.

The CERA-20C reanalysis does not capture the 1939 event. It also fails to adequately simulate the interannual variability, with a correlation with the AWAP analysis of $r = 0.6 \pm 0.1$ since 1910 and only slightly higher for start dates after 1940. The CERA-20C reanalysis also shows a cooling trend in heat extremes in this region over the period 1900–1970. This is in stark contrast to actual temperature observations, which are not assimilated in this reanalysis. Further investigation shows that this long-term cooling trend CERA-20C is a local effect in southeastern Australia (not shown). We suspect this unrealistic trend is caused by the increase of ocean observations that are assimilated over the course of the twentieth century, which may have caused a shift from states close to the reanalysis model climatology to states closer to reality.

The older ERA-20C reanalysis has even more unrealistic interannual variability of TX7x in southeastern Australia, with correlations of $r = 0.5 \pm 0.1$ with AWAP, independent of start date, which indicates hardly any coherence with the observed interannual variations in TX7x. It also shows systematically overestimated temperatures before 1915. Excluding those early years, the 1939 event is the warmest in this dataset, but not as warm as observed.

We further compare monthly mean temperature anomalies of January 1939 daily mean temperature, as for this quantity more datasets are available. The results are shown in Fig. S3. It shows that, as for TX7x, the anomalous heat occurred mainly inland. Global Historical Climatology Network Monthly (GHCN-M, Vose et al., 1992) v3 stations show anomalies of about 4°C in the bushfire region. The ACORN monthly analysis reproduces this well, as does the CRU TS 4.03 dataset (Harris et al., 2014), albeit with a lower amplitude due to greater spatial smoothing. On this monthly timescale it is also reproduced well by Berkeley Earth, but underestimated by the 20CRv3 reanalysis. The CERA-20C reanalysis does not show any substantial anomalies in this region at that time and is again clearly unrealistic. The ERA-20C is about halfway between this and the observations in terms of amplitude.

Considering all this evidence, we disregard the Berkeley Earth dataset and the CERA-20C and ERA-20C reanalyses for the weekly heat extremes (TX7x) attribution in this study and just use AWAP, JRA55, 20CRV3, and ERA5.

As described in section 2.4, the trend and return period are calculated using the properties of the fit of a Generalized Extreme Value (GEV) distribution, in which the location parameter varies linearly with the smoothed Global Mean Surface Temperature (GMST). As the domain has not been selected on the basis of temperatures we include the year 2019/20 in the fit for TX7x when available in the datasets. We note that the TX7x GEV distributions have a negative shape parameter, which implies that an upper bound exists for the distribution. Hence if the observed 2019/20 event lies above the upper bound of the distribution in 1900, the probability of the event occurring without the GMST trend is zero, and the increase in likelihood due to global warming is formally infinite, although the 95% confidence interval usually has a finite lower bound.

S1.4 Observational analysis: return time and trend

In the AWAP series the 2019/20 TX7x value over the study domain is 35.9 °C, the third-highest value after 1938/39 and 2018/19. It has a return time of about 8 yr (5 … 35 yr), which we use to define the thresholds in reanalyses and models. For

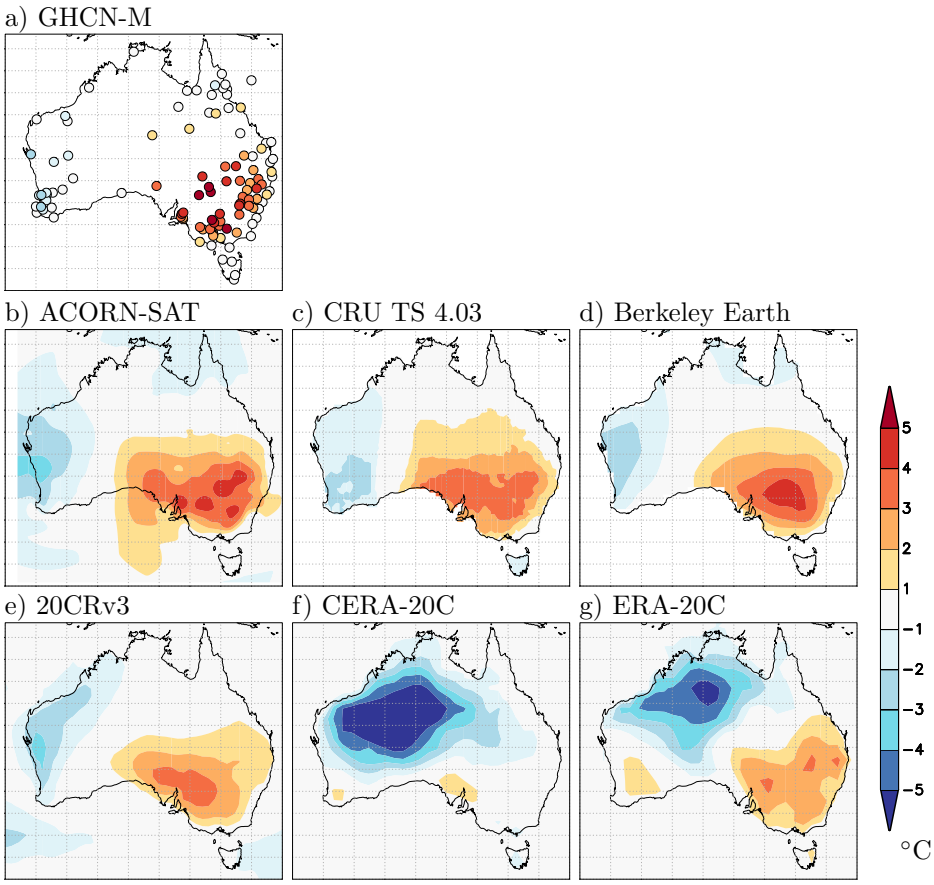

Figure S3. The Australian monthly mean daily mean temperature anomalies relative to 1981–2010 in a) GHCN-M v3 station data, b) the ACORN-SAT analysis, c) the CRU TS 4.03 analysis, d) the Berkeley Earth analysis, e) the 20CRv3 reanalysis, f) the CERA-20C reanalysis (ensemble mean) end g) the ERA-20C reanalysis.

the year 1900, the GEV fit of the AWAP data gives a return time of 85 yr (35 … ∞ yr) (see Fig. S4, which implies that the probability for an event like the 2019/20 event or warmer has increased by a factor of about 11 (3 … ∞) from 1900 to 2019. TX7x itself has increased by about 1.7 °C (0.8 … 2.6 °C) on average over this period. JRA-55, extrapolated to 1900, tells a similar story, with a significant temperature increase of 1.5 (1.3…3.4) °C from 1900 to 2019. As the 20CRv3 reanalysis does not assimilate near-surface temperatures we do not expect the quantitative results for TX7x to reflect reality, but note that qualitatively they agree well with the other estimates of the observations. Finally, ERA5 shows a larger trend over the much shorter period 1979–2018, 3.3 (1.8…4.7) K/K. However, due to the larger uncertainties associated with trends in the short ERA5 dataset, this is still compatible with the long-term trends in other datasets. Still, as the period over which the trend is estimated differs strongly from the observations and models we do not show results from this ERA5 in the summary plots. We base the rest of the analysis on the AWAP results and show the ACORN stations, 20CRv3 and JRA-55 results to show

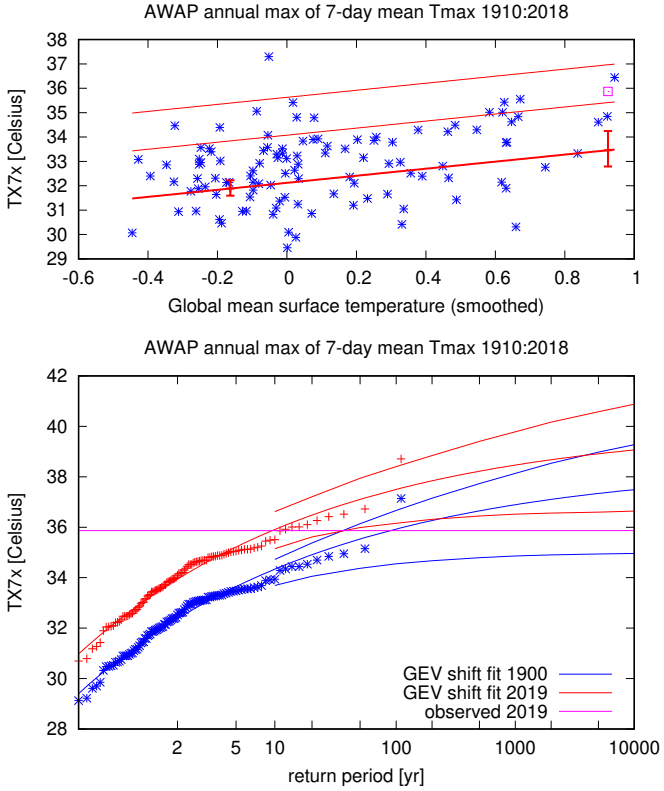

Figure S4. GEV fit to the AWAP TX7x averaged over the bushfire region. The position parameter μ is assumed linearly dependent on the smoothed GMST and the scale and shape parameters are constant. Top: observations (blue symbols), location parameter μ (thick line) and the 6 and 40 yr return values (thin lines). Bottom: return time plot with fits for the climates of 1900 (blue lines with 95% confidence interval) and 2019 (red lines), the purple line denotes the 2019/20 event. The observations are plotted twice, shifted down to the climate of 1900 (blue stars) and up to the climate of 2019 (red pluses) using the fitted dependence on smoothed global mean temperature so that they can be compared with the fits for those years.

that these are similar even though they are based on different data sources, building confidence in the primary results based on AWAP.

S1.5 Model evaluation

We consider a set of eight climate model ensembles that had daily maximum temperatures available to carry out the attribution analysis. To investigate whether the models represent extreme heat well, we compare the fit parameters of the tail of the TX7x distribution of the models with those of the observations. In this GEV fit we take the smoothed observed global mean temperature as covariate. The results are shown in Fig. S5. The model results have smaller uncertainties due to natural variability as they have multiple ensemble members, compensating for the sometimes shorter length (see Table 1).

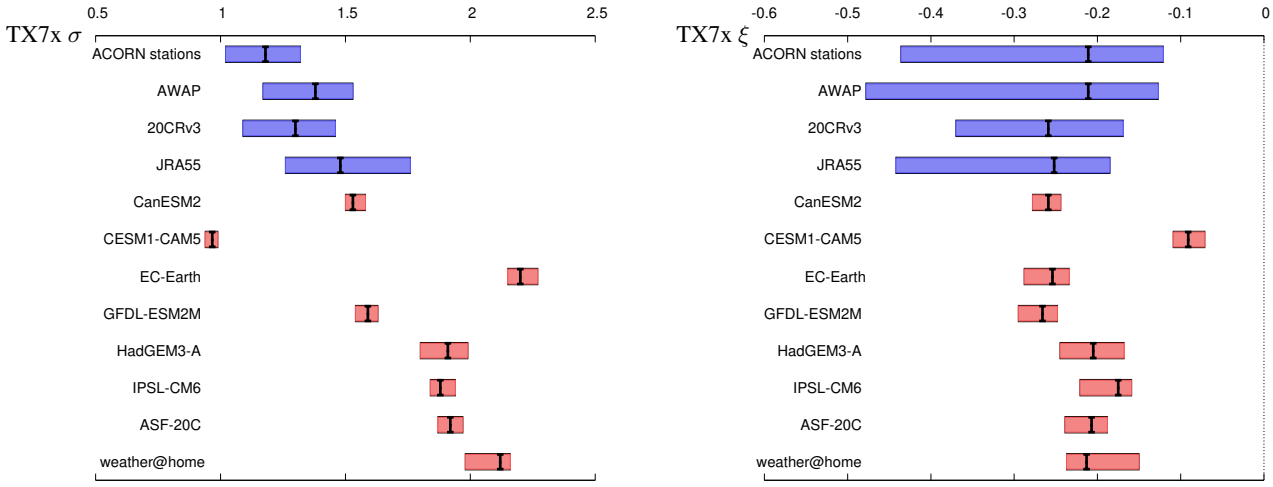

Figure S5. Left: scale parameter σ (K) in GEV fits of TX7x in observations, reanalyses and climate models. Right: same for the shape parameter ξ.

The comparison between the fit values of the observations and the models shows that most models overestimate the scale parameter σ. This corresponds to the models having too much variability for TX7x. The same problem was found in the Mediterranean (Kew et al., 2019) and northwestern Europe (Vautard et al., 2020). The only exception is the CESM1-CAM5 model, whose scale parameter is too small. This model also has a shape parameter ξ that is incompatible with the fit to observations, all other models agree with the observations in this parameter.

These discrepancies between models and observations implies that we cannot give quantitative results for the attribution of heat extremes in southeastern Australia, as the heat extremes in the climate models are too different from the observed heat extremes. This affects especially the change in probability, which depends strongly on the variability. For the trend estimates the influence of this shortcoming is smaller. We continue with all models apart from CESM1-CAM5, keeping these limitations in mind.

S1.6 Multi-model attribution and synthesis

We computed trends in the models by either comparing the actual climate 1987–2017 to an estimate of a counterfactual climate of the same period with anthropogenic emissions (weather@home) or by fitting a scaled distribution to the transient data in the same way as for the observational estimates, using the observed smoothed GMST (all other climate models) as covariate. This revealed one outlier: the ASF-20C ensemble has a negative trend over the full 1901-2010 period, so we only use data from 1960 onwards.

Fig. S6 summarises the change in probability and in intensity since 1900 for the 2019 event (observations) and a 10-yr event (the remaining seven models). The observations indicate a 1 to 2 °C temperature increase, with a return time of about 10 years.

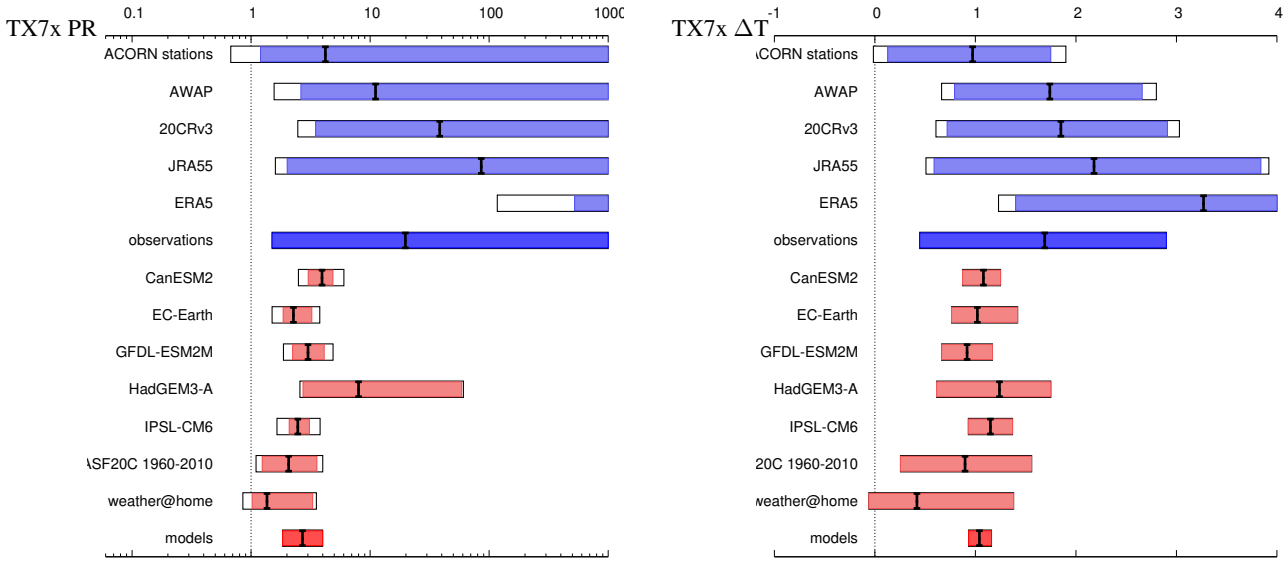

Figure S6. Synthesis plots of the Probability Ratio PR (left) and change in temperature ΔT (Celsius, right) in TX7x between 1900 and 2019 for the observations (blue), models (red). ERA5 is not included in the observational synthesis due to its much shorter time period. We do not attempt an overall synthesis as the models disagree too much with the observations.

In contrast, the models only simulate about 1 °C. The value for 1900 is determined by extrapolating the statistical fit to the data available. Note that this extrapolation represents a small fraction of the total trend due to the majority of GMST change between 1900 and the present day occurring after 1970.

Several observational and reanalysis datasets (ACORN stations, CERA-20C) and one model (ASF-20C) display what appears to be a non-stationary relationship between TX7x and GMST; as the starting time of a linear regression between them is varied from 1910 onwards, the best-estimate trend increases. For the ACORN stations this is probably due to the varying station coverage, with the trend over the stations active over the early part being smaller, maybe more coastal, than over the later part of the historical record. CERA-20C was excluded for not reproducing the 1939 event and ERA-20C for unrealistic trends and very little coherence with observed interannual variability in this area. ASF-20C is initialized from ERA-20C and run with the same SST dataset as boundary forcing (HadISST.2.1.0.0) (Weisheimer et al., 2017) and hence shows similar weaknesses as this reanalysis. It agrees well with the observations over the satellite era, but has an unrealistic negative temperature trend over the whole century. This is heavily influenced by the too warm years at the beginning, but in fact the trend is negative for start dates as late as 1935 and only becomes comparable to the observations and reanalysis from around 1960 onwards (not shown). We do not know what causes the long-term trends to be at odds with observations in southeastern Australia.

In the period before 1950 the global mean temperature was affected as much by volcanic and other natural forcings as it was by greenhouse gases, with possibly different effects from the anthropogenic forcings on circulation. Observations were also less numerous and reliable before 1950. We therefore also show a figure with results using data just from 1950 onwards,

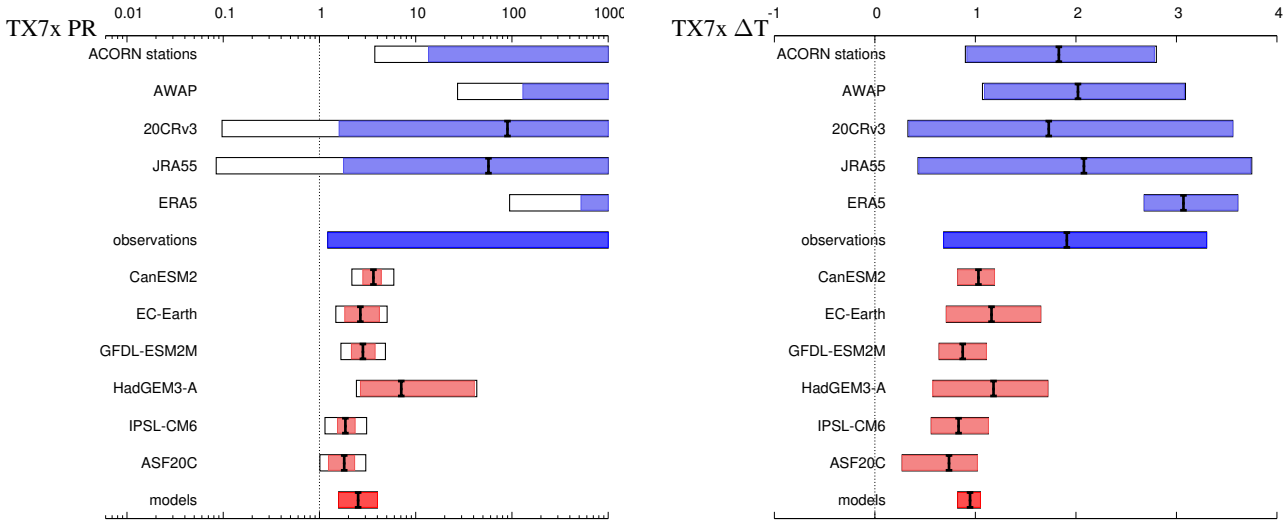

Figure S7. As Fig. S6 but using only data starting in 1950.

Fig. S7, noting that this is also a better estimate of the greenhouse-gas driven trend with better observations than the whole period since 1900. The shorter time period allows us to include ERA5, but we cannot define this for the weather@home model that has a difference between the actual climate and a counterfactual climate without anthropogenic emissions. The statistical uncertainties are larger due to the shorter time period. The agreement of these results with Fig. S6 shows that the changes are mainly due to anthropogenic forcings, while the lower quality or coverage of observations before 1950 does not influence the general results.

There are two interpretations of the discrepancy in trends between the observations and models: either the observations are influenced by another driver than anthropogenic climate change that caused the rapid rise in extreme temperatures, or the models have problems simulating the response of of TX7x to external forcing and their related processes (or a combination of these two). As long as it is unknown which of the two explanations is correct we can only quote a lower bound on results.

The Probability Ratios are roughly ten in the observational datasets, with lower bounds as low as a two (Fig. S6). The model results are heavily influenced by the overestimated variability: the high variability in the model, together with the low trends, induces lower probability ratios than in the observations. As there is no overlap between the observed and simulated values we do not attempt to synthesise the results but only quote a lower bound. The spread in the models is compatible with their estimates of natural variability ($\chi^2/\mathrm{dof} \approx 1$) so we compute a weighted average. This results in an increase in probability between 1900 and 2019 of a factor three with a lower bound of a factor two.

S1.7 Conclusions extreme heat

We analysed the highest 7-day mean maximum temperatures of the year (TX7x) averaged over the event domain. Observations show that a heatwave as rare as observed in 2019/20 would have been 1 to 2 °C cooler at the beginning of the 20th century. Similarly, a heatwave of this intensity would have been less likely by a factor of about 10 in the climate around 1900.

While eight climate models simulate increasing temperature trends they all have some limitations for simulating heat extremes: the variability is in general too high and the trend in these heat extremes is only 1 °C. We can therefore only conclude that anthropogenic climate change has made a hot week like the one in December 2019 more likely by at least a factor of two. As is shown in section 6 the variability explained by the Indian Ocean Dipole (IOD) and Southern Annual Mode (SAM) is too small to explain these mismatches as problems in the model representation of these modes. The literature suggests that shortcomings in the coupling to land and vegetation (e.g. Fischer et al., 2007; Kala et al., 2016) and in parametrisation of irrigation (e.g. Thiery et al., 2017; Mathur and AchutaRao, 2019) in the exchange of heat and moisture with the atmosphere, and also in the representation of the boundary layers (e.g. Miralles et al., 2014) are more likely to be the cause of the problems. Given the larger trend in observations in the models, we suspect that climate models underestimate the trend due to climate change, although in principle the difference could also be due to a non-climatic driver with a trend, affecting the observations. Coupled with the high variability of the models, the increase in the likelihood of such an event to occur is likely much higher than the models simulate.

S2 Meteorological drought

S2.1 Temporal Event Definition

Here, we analyze meteorological drought, using two timescales. The first one is annual drought, the second one the driest month in the fire season September–December. Due to the large variability in precipitation and the low number of events compared with, e.g. hot weeks, drought trends can only be detected and attributed reliably over long time periods. Model dependencies are also large so we need a large model ensemble. We therefore use monthly mean data starting in 1900 as more models provide monthly data than daily data. Note that mean monthly precipitation in the study area is almost constant through the seasonal cycle, but inter-monthly variability is very large compared to the mean, σ/μ = 49% on average, larger in summer and smaller in winter.

The 2019 January–December annual mean was Australia's driest year on record since 1900 (Bureau of Meteorology, Annual Climate Statement 2019). This was also the case in our study region in southeastern Australia with an annual total of 467 mm against a 1900–2019 climatology of 825 mm. The two previous years had also been very dry, but we could not find evidence that this still affected the 2019/20 bushfires: the correlation between the logarithm of MODIS area burned in our study domain during September–February and precipitation in the three preceding years is very low ($r = -0.01$ against -0.74 for simultaneous precipitation and -0.49 for the preceding annual precipitation). Annual precipitation also does not show a significant lag-1 autocorrelation which would support the idea of coherent and somewhat regular multi-year droughts ($r =$

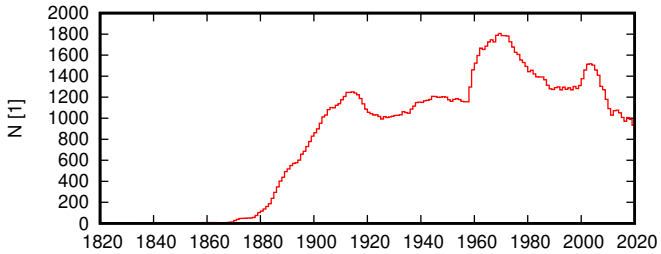

Figure S8. Number of Global Historical Climatology Network-Daily (GHCN-D, Menne et al., 2016) daily precipitation stations with at least 10 years of data in the study area.

0.15). We therefore analyse annual mean droughts but not multi-year droughts. For the second temporal definition, the driest month of the fire season, December 2019 was one of the driest months on record in the study region since 1900.

S2.2 Observational precipitation data and methods

We considered three observational datasets of monthly precipitation: Global Precipitation Climatology Centre (GPCC) v18 1900–2018 (Schneider et al., 2018b) extended with the monitoring analysis (Schneider et al., 2018a) up to November 2019 and the first guess analysis (Ziese et al., 2011) up to January 2020, the (CRU TS 4.03 1901–2017 (Harris et al., 2014) and AWAP 1900–January 2020 (Bureau of Meteorology data). As the distributions of annual mean precipitation and the driest month in the fire season are both not described well by a Gaussian, we use a GPD fit to the lowest 20% or 30% for the observations. In the fit we enforce that the distribution has a lower bound ($\xi < 0$) that is larger than zero ($\sigma < -\xi u$) so that there is no probability for negative precipitation.

Figure S8 shows the number of stations in the GHCN-D dataset in the study region as a function of time. In contrast to the temperature observations, the number of rain gauges is relatively constant and very high starting around 1900, so differences in station density do not influence the results as much as for temperature. In contrast to the temperature analyses of Section S1, the systematic differences between the different datasets are smaller than the uncertainties due to the natural variability. We take these into account by analysing three observational datasets.

S2.3 Observational analysis: return time and trend

For the annual mean low precipitation analysis, the fit for AWAP data using the lowest 20% is shown in Fig. S9. The year 2019 is not included in the fit. This fit shows a significant trend towards more extreme dry years over the period 1900-2018. The 2019 return time of 16 yr (3 . . . 550 yr) is the lowest in the observational datasets. The fit should ideally be independent of the threshold used to define 'low precipitation', but this is not the case: whereas the lowest 20% show a significant downward trend, the GPD fit to the lowest 30% has an upward trend that is not significant at $p < 0.05$ (two-sided) in the AWAP dataset (Fig. S9, right). The lowest 10% does not contain enough data to fit a GPD. We report both the 20% and 30% choices in the following to include the uncertainty due to the choice of threshold.

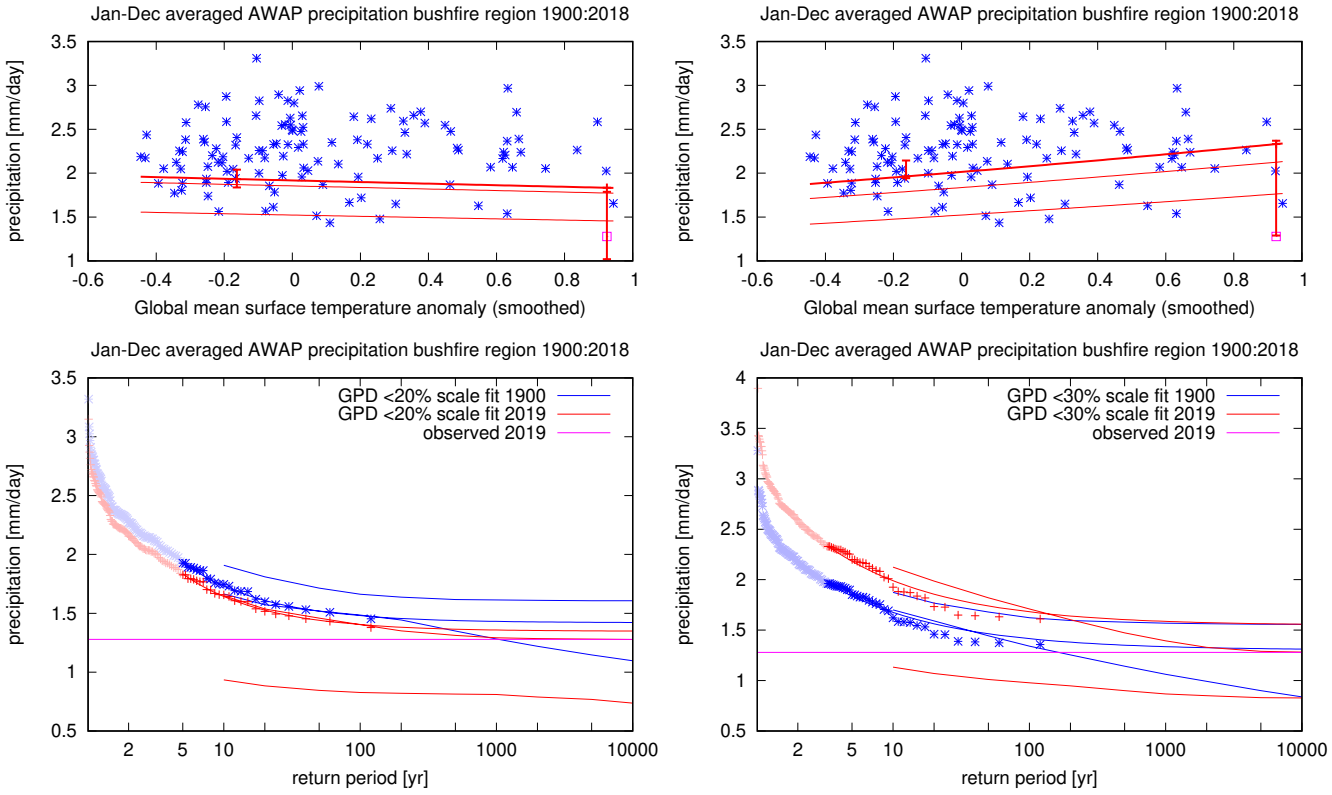

Figure S9. GPD fits to the AWAP estimate of annual mean precipitation in the bushfire region. The position and scale parameters depend exponentially on the observed smoothed global mean surface temperature such that their ratio is constant. The scale parameter is forced to be negative and the cut-off is forced to be zero or higher. Left: using the lowest 20%. Right: using the lowest 30%. Top: observations (blue symbols), threshold u (thick line) and the 6 and 40 yr return values (thin lines). Bottom: return time plot for the climates of 1900 (blue) and 2019 (red) with 95% confidence intervals. Light colour symbols are below the threshold and the purple line denotes the 2019/20 event.

The return time of the annual low 2019 precipitation depends strongly on the observational dataset and the cut-off in the GPD fit. Using the 30% driest years it ranges from 25 yr (3 . . . 4000 yr) in GPCC to infinity in AWAP. As usual for precipitation analyses, the uncertainty ranges are large (e.g. 3 . . . 3000 yr for GPCC 20%). The uncertainty ranges are in fact more similar between GPCC 20% and 30% than their best fit values. Given that it was the lowest value in 120 years, we use a return time of 100 yr to find the corresponding thresholds in the climate models.

We also fit a GPD to the lowest 20% and 30% of monthly precipitation amounts in the fire season September–February. These extremes are more difficult to fit because the values can approach zero. In fact, in some bootstrapped time series no initial conditions for the fit routine could be found that satisfy all constraints. The result is that the uncertainty range is too small for some fits and does not encompass the best fit. This weakens the robustness of the parameter estimates.

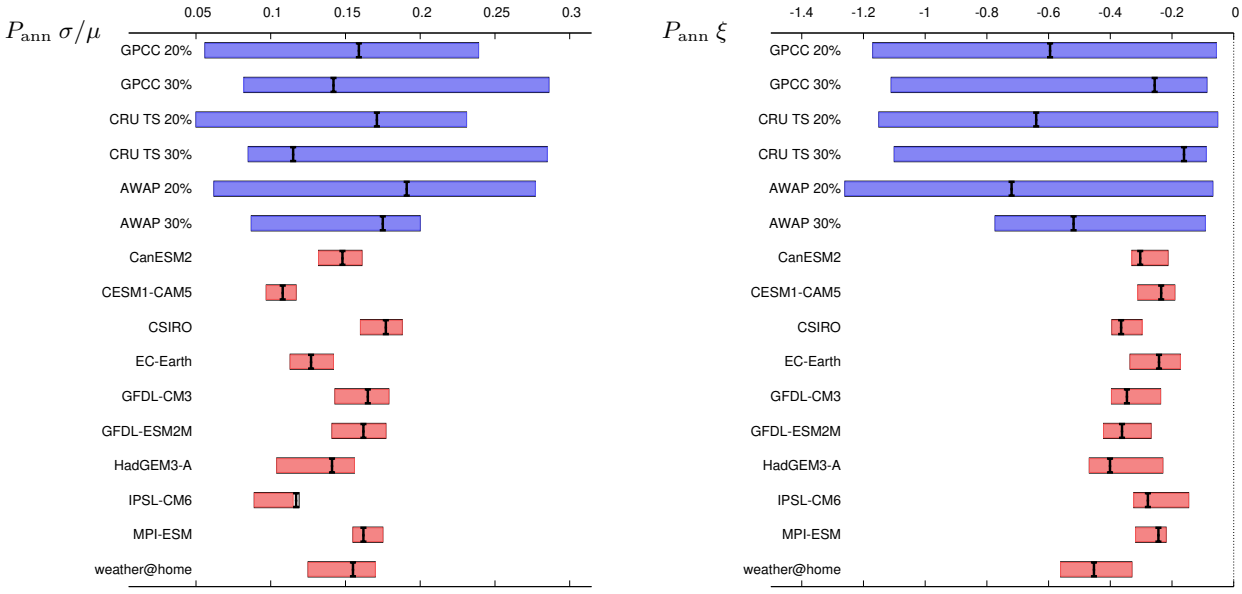

Figure S10. The dispersion parameter σ/u (left) and shape parameter ξ (right) of GPD fits to the low tail of the annual mean precipitation distribution in observations (blue, lowest 20% and 30%) and models (red, lowest 20%).

The driest month in 2019/20 was December 2019 with 0.49 mm/dy (15 mm/mo) against a climatological value for December 1900–2019 of 2.44 mm/dy (76 mm/mo). The return times obtained from the fits again vary widely, from 75 yr (15 . . . 200 yr) to 800 yr (10 . . . 250 yr), both for the GPCC analysis for the 20% and 30% thresholds. To find the corresponding threshold in the models we thus use a return time of 100 yr.

S2.4 Model evaluation

As discussed above, we consider the annual mean drought and driest month of the fire season for ten climate model ensembles. The ASF-20C model only has 4-month runs starting four times per year and therefore cannot provide continuous and physically consistent annual or 6-month fire season precipitation, as slowly varying land boundary conditions such as soil moisture are discontinuous every three months when a new ensemble is initialized. Using this dataset without significant further investigation is therefore not straightforward and led us to exclude it from our analysis.

The statistical description of the low tail of annual mean precipitation in all models agrees with the same quantities in the observations within the (large) uncertainties due to natural variability (Fig. S10).

Similarly, for the driest month in the fire season all models have statistical descriptions of the low tail of the distribution that agree with the description of the observed tail within the large uncertainties of the various observational estimates (Fig. S11).

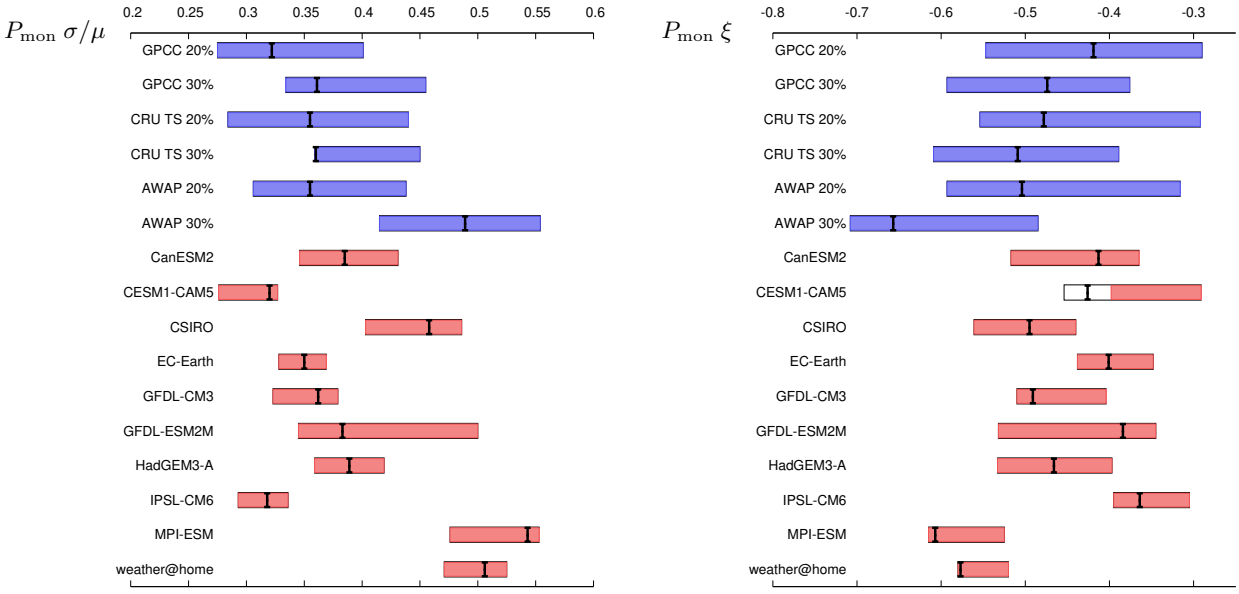

Figure S11. As Fig. S10 but for the driest month in the fire season September–February. The bootstrapped uncertainty intervals are sometimes underestimated due to fitting problems.

S2.5 Multi-model attribution and synthesis

Fig. S12 shows the change in probability and intensity of annual mean drought averaged over the study region. The observations show a positive probability ratio PR and smaller intensities of low precipitation events, which implies a shift towards a larger probability for drought over the last 120 years. However, the models show no trend, so we cannot attribute these shifts to anthropogenic climate change. The observed trends can be due to natural variability (note that the 95% uncertainties encompass zero and these ignore the year-to-year autocorrelations, the lag-1 autocorrelation is borderline significantly different from zero but still very small, $a_1 \approx 0.2$, so the true uncertainties are slightly larger). Another possibility is that they are due to other drivers not included in this analysis. Finally, the difference could again be due to shortcomings in the climate models. Note that the large natural variability can hide such potential shortcomings in the model evaluation in section S2.4.

Following Otto et al. (2018) we investigate whether the lack of trend in the models is just due to high natural variability masking a potential underlying trend by repeating the analysis using data up to 2100 for all models that also have future data (CanESM2, CESM1-CAM5, CSIRO Mk3.6.0, EC-Earth, GFDL CM3, GFDL ESM2M, MPI ESM), using the model ensemble-averaged GMST as covariate. This reduces internal variability and reveals model differences more clearly. Nevertheless, model trends are between -7% and $+7\%$, showing no systematic trend towards more dry extremes (not shown). It should be noted that individual models show large trends towards less mean annual precipitation, in contrast to the lowest 20% and 30% of annual precipitation values, which do not show such trends.

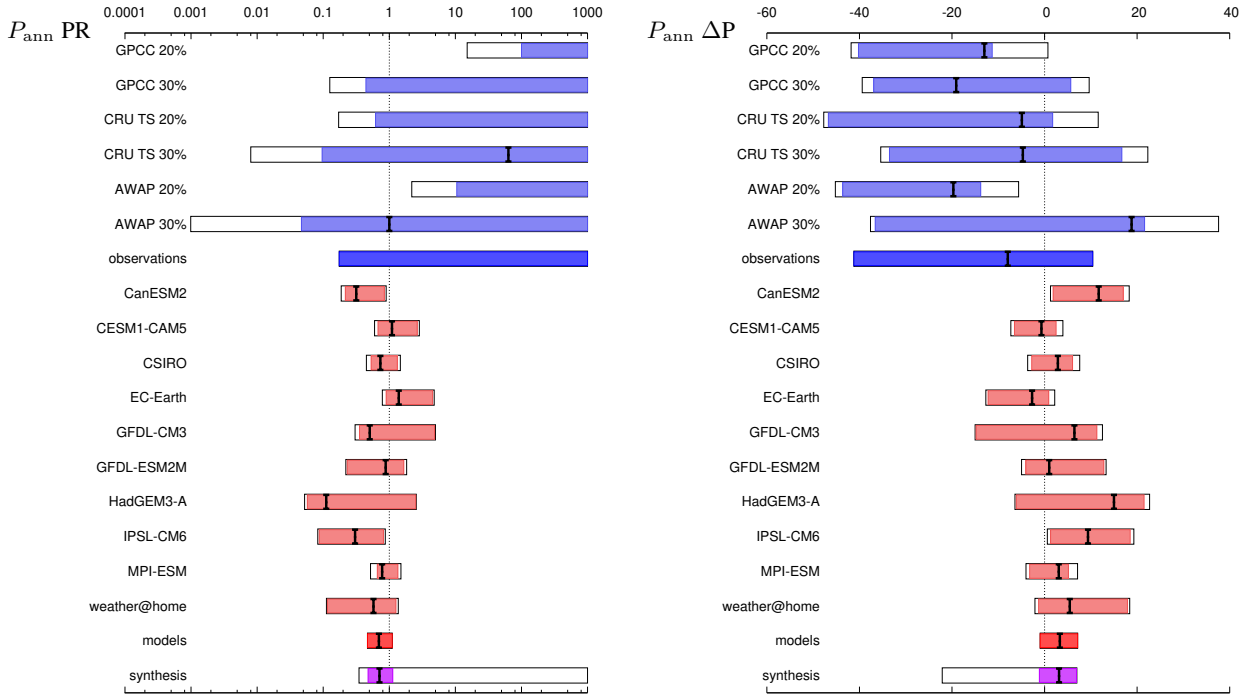

Figure S12. PR (left) and ΔP (%) (right) for annual mean low precipitation. The purple bar indicates the weighted average under the assumption that the model spread is equal to the model uncertainty, the white box around this purple bar gives equal weight to the observations and models.

The synthesis for the driest month of the fire season is shown in Fig. S13. Although the fits are not very good, both observations and models indicate a small, non-significant increase in precipitation, which is equivalent to a decrease in probability to observe as dry a month as December 2019 (PR < 1). Due to the fact that the uncertainties in the PR and ΔP encompass zero, there is no attributable trend in the occurrence of very dry months in the fire season.

S2.6 Conclusions meteorological drought

Observations show non-significant trends towards more dry extremes like the record 2019 annual mean and a non-significant trend towards fewer dry months like December 2019 in the fire season. All ten climate models we considered simulate the statistical properties of the observations well. Collectively they show no trend in dry extremes of annual mean precipitation nor in the driest month of the fire season (September–February). We conclude that there is no evidence for an attributable trend in either kind of dry extremes like the ones observed in 2019.

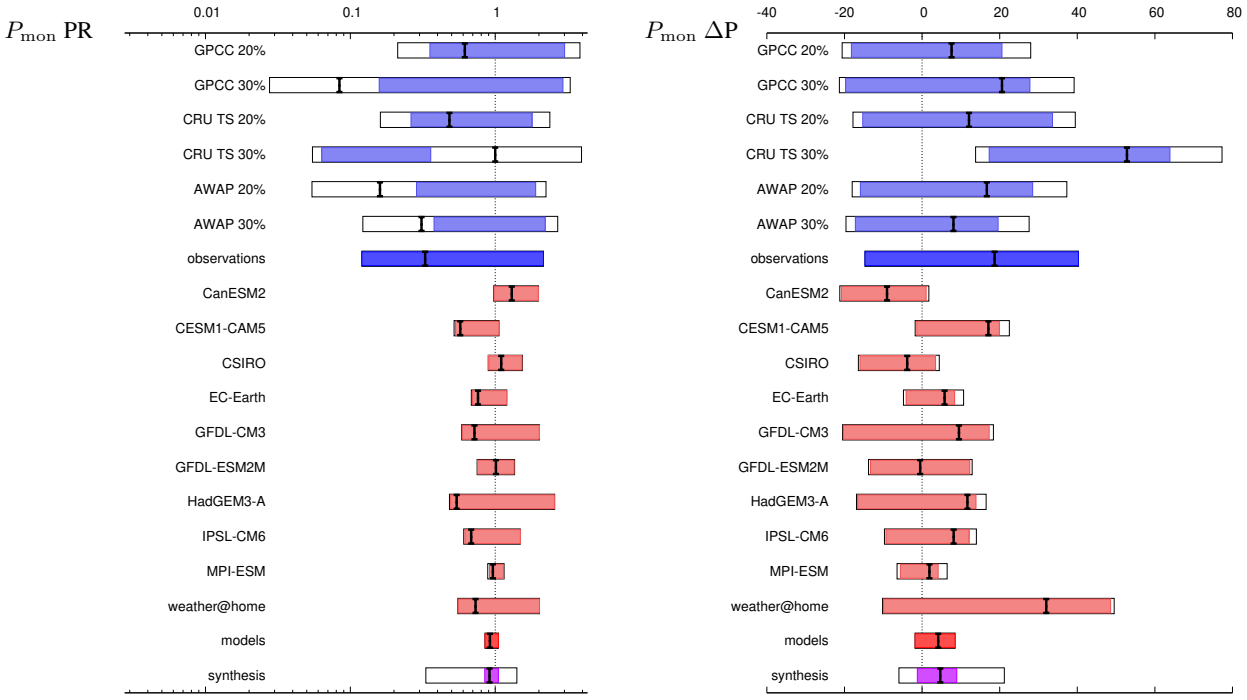

Figure S13. PR (left) and ΔP (%) (right) for the driest month in September–February. The purple bar indicates the weighted average under the assumption that the model spread is equal to the model uncertainty, the white box around this purple bar gives equal weight to the observations and models. For most observational datasets and some models the uncertainty range is underestimated due to problems fitting the data, this is taken care of in the averages by increasing the representation error and model spread terms (white boxes).

S3 Other drivers

There are known associations between large-scale climate drivers, such as El Niño—Southern Oscillation (ENSO), the Indian Ocean Dipole (IOD) and the Southern Annular Mode (SAM), and fire risk (e.g. Williams and Karoly, 1999; Cai et al., 2009; Harris and Lucas, 2019; King et al., 2020). These drivers of interannual variability can dominate the risk of fire weather over the trend in individual years (Harris and Lucas, 2019). Note that the influence of these drivers is automatically included in the analyses presented so far. Here, we briefly investigate how they influenced some of the fire weather variables in the particular event of the summer of 2019/20.

S3.1 ENSO

ENSO variations are linked to Australia's climate variability, with generally warm and dry conditions in eastern Australia during El Niño, although the signal is weaker on the east coast. ENSO was considered neutral during 2019/20, however, the western Pacific was anomalously warm. In fact, the relative Niño4 index, an index in which the long-term climate change

influence is removed (van Oldenborgh et al., 2020), indicated El Niño conditions of the Central Pacific 'flavour' (Ren and Jin, 2011) with a value around +0.6 °C during the 2019/20 fire season. The atmospheric state was also typical for weak El Niño conditions with the Southern Oscillation Index (SOI) of the National Centers for Environmental Prediction (NCEP) at around -0.6 until December 2019, perhaps encouraging an enhancement of the IOD via atmospheric teleconnections (Cai et al., 2011).

S3.2 Indian Ocean Dipole

The IOD is an interaction between the ocean and atmosphere in the tropical Indian Ocean basin with climatic influences around this basin (Saji et al., 1999). In general, IOD events develop in the Southern Hemisphere winter through spring, and break down with the start of the Indonesian monsoon in early summer. It is thus not an important driver through summer. In the positive phase, colder than normal sea surface temperatures are observed in the eastern Indian Ocean (around Sumatra and Java). Positive IOD events are typically associated with below average winter-spring rainfall in Southern Australia and warmer than average conditions (White et al., 2014). As a result, IOD positive phases are associated with severe bushfire conditions (Harris and Lucas, 2019; Cai et al., 2009).

In 2019, an unusually strong positive IOD event was observed, which, together with a strong negative excursion of the Southern Annular Mode, was argued to be primarily responsible for the precipitation deficit over southeastern Australia (King et al., 2020). This event started to emerge in June but matured and strengthened during early austral Spring. The late onset of the monsoon off Sumatra also led to the unusual persistence of the IOD into early summer in 2019. Here we use the Dipole Mode Index, DMI based on the Extended Reconstructed Sea Surface Temperature (ERSST) v5 analysis. Because of uncertainties whether the upwelling zone was measured correctly we only use data starting in 1958. Variations in the IOD explain only a small fraction of variance in observed temperatures. In particular, the correlation with the AWAP TX7x index defined in section S1 is only $r = 0.13$ for the September–October averaged DMI index and $r = -0.14$ for December–February (Fig. S14a), neither is significant at $p < 0.1$.

The correlation with the AWAP precipitation in July–December is higher, $r = -0.4$. This does include some double-counting in the statistical relation: as the IOD is often partially forced by ENSO, thus a fraction of these correlations are in fact ENSO teleconnections. When the influence of ENSO teleconnections, expressed as the regression on the relative Niño3.4 index, is linearly removed from the DMI, these correlations become much lower, with no significant connection with TX7x and a correlation of $r = -0.18$ with July–December rainfall (Fig. S14). However, even with this low correlation, the very high positive IOD conditions observed in July-December 2019 account for approximately one third of the July-December low rainfall, see Fig. S14. We chose this half year as it precedes the fire season September–February and therefore represents some of the drought preconditioning measured by the fire weather risk indices used in the main paper. As the Niño3.4 index was neutral during the second half of 2019, it did not contribute to the drought during that part of the year, although as mentioned above, western Pacific SST and the atmospheric circulation did indicate a weak El Niño during the second half of 2019.

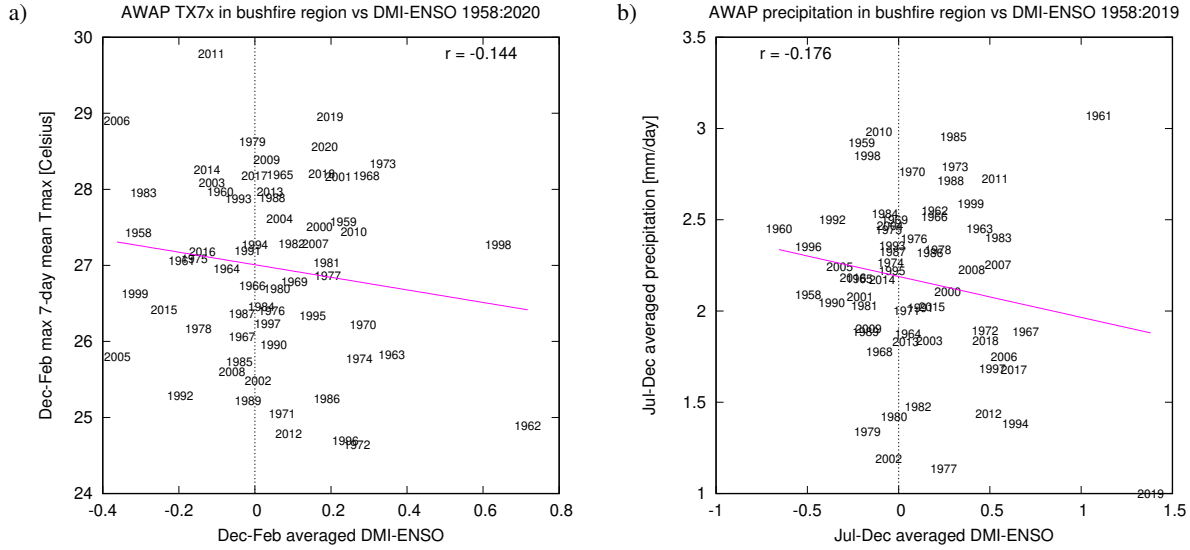

Figure S14. Scatterplots of a) December–February AWAP TX7x and b) July–December AWAP precipitation averaged over the bushfire region in southeastern Australia as a function of the DMI index based on ERSST v5 with the monthly linear regression on the relative Niño3.4 index subtracted over the same months, 1958–2019.

S3.3 Southern Annular Mode and stratospheric preconditioning

The Southern Annular Mode (SAM) is an important mode of climate variability in the Southern Hemisphere related to variations in the large-scale atmospheric circulation. The positive phase of the SAM is associated with a stronger and more contracted stratospheric polar vortex and a stronger and more poleward located mid-latitude storm track. The impact of the SAM on the Australian climate variability is seasonally dependent and opposite precipitation responses are found in different regions of the continent. Based on ERA-Interim reanalysis data, a strong negative subtropical precipitation response during spring and summer in southeastern Australia has been found for the negative phase of the SAM (Hendon et al., 2014). This relationship still holds when the influence of ENSO is removed from the SAM index, although it becomes somewhat weaker, with $r = 0.34$ (Fig. S15b). During most of the second half of 2019 (July–December) the SAM phase was negative, with the most negative values in November 2019. This negative phase of the SAM during 2019 has contributed roughly another one third to the extreme drought conditions in southeastern Australia from July to December (Fig. S15). We did not find a significant correlation of SAM with our measure of heat waves, TX7x, which is in in agreement with Perkins et al. (2015): $r = -0.07$, Fig. S15a.

We verified that the statistics of 10–100 yr low extremes of the Southern Annular Mode averaged over July–December are represented well in the models used for the attribution analysis except CESM1-CAM5 (scale parameter too small) and weather@home (data not available).

The strong negative SAM excursion of 2019 was very well predicted. One cause was a Sudden Stratospheric Warming (SSW) event, where the winter stratospheric vortex over Antarctica breaks down and the stratosphere warms rapidly. These are

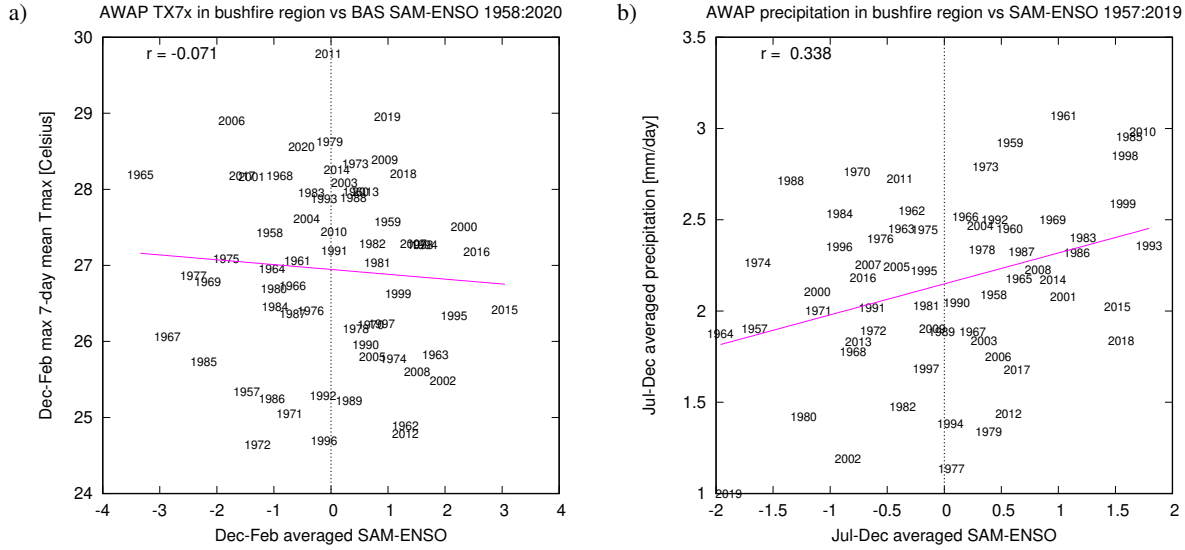

Figure S15. Scatterplots of a) December–February AWAP TX7x and b) July–December AWAP precipitation averaged over the bushfire region in southeastern Australia as a function of the SAM index.

rare events, with only two major events recorded, in 2002 and 2019. In 2019, the negative phase of the SAM from October onwards has been preconditioned by the preceding SSW event through a downward coupling of the weakened polar vortex to tropospheric levels as highlighted by Lim et al. (2020). SSW events are thus associated with warm and dry conditions over eastern Australia (Lim et al., 2019).

Another interconnected cause of the record SAM state was the strong positive ozone anomaly in September, associated with a relatively warm polar stratosphere and an exceptionally weak ozone hole season (UNEP, 2019). This was followed by a period with a negative phase of the SAM from October onwards which is in line with the ozone-SAM correlations found by Son et al. (2013); Lim et al. (2018); Byrne and Shepherd (2018).

S3.4 Conclusions other drivers

The attribution statements presented in this paper are for events defined as meeting or exceeding the threshold set by the 2019/20 fire season and thus assessing the overall effect of human-induced climate change on these kinds of events. In individual years, however, large-scale climate system drivers can have a higher influence on fire risk than the long-term trend.

Besides the influence of anthropogenic climate change, the particular 2019 event was made much more severe by a record positive excursion of the Indian Ocean Dipole and a very strong negative anomaly of the Southern Annular Mode, which likely contributed substantially to the precipitation deficit. We did not find a connection of either mode to heat extremes. More quantitative estimates will require further analysis and dedicated model experiments, as the linearity of the relationship between these indices and the regional climate is not verifiable from observations alone.

References

Byrne, N. J. and Shepherd, T. G.: Seasonal Persistence of Circulation Anomalies in the Southern Hemisphere Stratosphere and Its Implications for the Troposphere, Journal of Climate, 31, 3467–3483, https://doi.org/10.1175/JCLI-D-17-0557.1, 2018.

Cai, W., Cowan, T., and Raupach, M.: Positive Indian Ocean Dipole events precondition southeast Australia bushfires, Geophys. Res. Lett., 36, https://doi.org/10.1029/2009GL039902, 2009.

Cai, W., van Rensch, P., Cowan, T., and Hendon, H. H.: Teleconnection Pathways of ENSO and the IOD and the Mechanisms for Impacts on Australian Rainfall, J. Climate of Climate, 24, 3910–3923, https://doi.org/10.1175/2011JCLI4129.1, 2011.

Cowan, T., Purich, A., Perkins, S. E., Pezza, A., Boschat, G., and Sadler, K.: More Frequent, Longer, and Hotter Heat Waves for Australia in the Twenty-First Century, J. Climate, 27, 5851–5871, https://doi.org/10.1175/JCLI-D-14-00092.1, 2014.

Fischer, E. M., Seneviratne, S. I., Vidale, P. L., Lüthi, D., and Schär, C.: Soil Moisture–Atmosphere Interactions during the 2003 European Summer Heat Wave, Journal of Climate, 20, 5081–5099, https://doi.org/10.1175/JCLI4288.1, 2007.

Harris, I., Jones, P. D., Osborn, T. J., and Lister, D. H.: Updated high-resolution grids of monthly climatic observations — the CRU TS3.10 Dataset, Int. J. Climatol., 34, 623–642, https://doi.org/10.1002/joc.3711, 2014.

Harris, S. and Lucas, C.: Understanding the variability of Australian fire weather between 1973 and 2017, PLoS ONE, 14, e0222 328, https://doi.org/10.1371/journal.pone.0222328, 2019.

Hendon, H. H., Lim, E.-P., and Nguyen, H.: Seasonal Variations of Subtropical Precipitation Associated with the Southern Annular Mode, Journal of Climate, 27, 3446–3460, https://doi.org/10.1175/JCLI-D-13-00550.1, 2014.

Hersbach, H., Bell, W., Berrisford, P., Horányi, A., J., M.-S., Nicolas, J., Radu, R., Schepers, D., Simmons, A., Soci, C., and Dee, D.: Global reanalysis: goodbye ERA-Interim, hello ERA5, ECMWF Newsletter, 159, 17–24, https://doi.org/10.21957/vf291hehd7, 2019.

Kala, J., De Kauwe, M. G., Pitman, A. J., Medlyn, B. E., Wang, Y.-P., Lorenz, R., and Perkins-Kirkpatrick, S. E.: Impact of the representation of stomatal conductance on model projections of heatwave intensity, Scientific Reports, 6, 23 418, https://doi.org/10.1038/srep23418, 2016.

Kew, S. F., Philip, S. Y., van Oldenborgh, G. J., Otto, F. E., Vautard, R., and van der Schrier, G.: The exceptional summer heatwave in Southern Europe 2017, Bull. Amer. Met. Soc., 100, S2–S5, https://doi.org/10.1175/BAMS-D-18-0109.1, 2019.

King, A. D., Pitman, A. J., Henley, B. J., Ukkola, A. M., and Brown, J. R.: The role of climate variability in Australian drought, Nature Climate Change, https://doi.org/10.1038/s41558-020-0718-z, 2020.

Kobayashi, S., Ota, Y., Harada, Y., Ebita, A., Moriya, M., Onoda, H., Onogi, K., Kamahori, H., Kobayashi, C., Endo, H., Miyaoka, K., and Takahashi, K.: The JRA-55 Reanalysis: General Specifications and Basic Characteristics, Journal of the Meteorological Society of Japan, 93, 5–48, https://doi.org/10.2151/jmsj.2015-001, 2015.

Laloyaux, P., de Boisseson, E., Balmaseda, M., Bidlot, J.-R., Broennimann, S., Buizza, R., Dalhgren, P., Dee, D., Haimberger, L., Hersbach, H., Kosaka, Y., Martin, M., Poli, P., Rayner, N., Rustemeier, E., and Schepers, D.: CERA-20C: A Coupled Reanalysis of the Twentieth Century, Journal of Advances in Modeling Earth Systems, 10, 1172–1195, https://doi.org/10.1029/2018MS001273, 2018.

Lewis, S. C. and King, A. D.: Dramatically increased rate of observed hot record breaking in recent Australian temperatures, Geophysical Research Letters, 42, 7776–7784, https://doi.org/10.1002/2015GL065793, 2015.

Lim, E.-P., Hendon, H. H., and Thompson, D. W. J.: Seasonal Evolution of Stratosphere-Troposphere Coupling in the Southern Hemisphere and Implications for the Predictability of Surface Climate, Journal of Geophysical Research: Atmospheres, 123, 12,002–12,016, https://doi.org/10.1029/2018JD029321, 2018.

Lim, E.-P., Hendon, H. H., Boschat, G., Hudson, D., Thompson, D. W. J., Dowdy, A. J., and Arblaster, J. M.: Australian hot and dry extremes induced by weakenings of the stratospheric polar vortex, Nature Geoscience, 12, 896–901, https://doi.org/10.1038/s41561-019-0456-x, 2019.

Lim, E.-P., Hendon, H. H., Butler, A. H., Garreaud, R. D., Polichtchouk, I., Shepherd, T. G., Scaife, A. A., Comer, R., Coy, L., Newman, P. A. ., Thompson, D. W. J., and Nakamura, H.: The 2019 Antarctic sudden stratospheric warming, SPARC newsletter, 54, 10–13, https://www.sparc-climate.org/wp-content/uploads/sites/5/2017/12/SPARCnewsletter_Jan2020_PRINT.pdf, 2020.

Mathur, R. and AchutaRao, K.: A modelling exploration of the sensitivity of the India's climate to irrigation, Climate Dynamics, https://doi.org/10.1007/s00382-019-05090-8, 2019.

Menne, M. J., Durre, I., Korzeniewski, B., McNeal, S., Thomas, K., Yin, X., Anthony, S., Ray, R., Vose, R. S., Gleason, B. E., and Houston, T. G.: Global Historical Climatology Network - Daily (GHCN-Daily), Version 3.22, https://doi.org/10.7289/V5D21VHZ, 2016.

Miralles, D. G., Teuling, A. J., van Heerwaarden, C. C., and Vilà-Guerau de Arellano, J.: Mega-heatwave temperatures due to combined soil desiccation and atmospheric heat accumulation, Nature Geoscience, 7, 345–349, https://doi.org/10.1038/ngeo2141, 2014.

Otto, F. E. L., Philip, S. Y., Kew, S. F., Li, S., King, A. D., and Cullen, H.: Attributing high-impact extreme events across timescales—a case study of four different types of events, Climatic Change, 149, 399–412, https://doi.org/10.1007/s10584-018-2258-3, 2018.

Perkins, S. E. and Alexander, L. V.: On the Measurement of Heat Waves, Journal of Climate, 26, 4500–4517, https://doi.org/10.1175/JCLI-D-12-00383.1, 2013.

Perkins, S. E., Argüeso, D., and White, C. J.: Relationships between climate variability, soil moisture, and Australian heatwaves, Journal of Geophysical Research: Atmospheres, 120, 8144–8164, https://doi.org/10.1002/2015JD023592, 2015.

Perkins-Kirkpatrick, S. E. and Gibson, P. B.: Changes in regional heatwave characteristics as a function of increasing global temperature, Scientific Reports, 7, 12 256, https://doi.org/10.1038/s41598-017-12520-2, 2017.

Ren, H.-L. and Jin, F.-F.: Niño indices for two types of ENSO, Geophysical Research Letters, 38, https://doi.org/10.1029/2010GL046031, 2011.

Rohde, R., Muller, R. A., Jacobsen, R., Muller, E., Perlmutter, S., Rosenfeld, A., Wurfele, J., Groom, D., and Wickham, C.: A New Estimate of the Average Earth Surface Land Temperature Spanning 1753 to 2011, Geoinformatics & Geostatistics: An Overview, 1, 1, https://doi.org/10.4172/2327-4581.1000101, 2013.

Saji, N. H., Goswami, B. N., Vinayachandran, P. N., and Yamagata, T.: A dipole mode in the tropical Indian Ocean, Nature, 401, 360–363, https://doi.org/10.1038/43854, 1999.

Schneider, U., Becker, A., Finger, P., Meyer-Christoffer, A., and Ziese, M.: GPCC Monitoring Product: Near Real-Time Monthly Land-Surface Precipitation from Rain-Gauges based on SYNOP and CLIMAT data, https://doi.org/10.5676/DWD_GPCC/MP_M_V6_100, 2018a.

Schneider, U., Becker, A., Finger, P., Meyer-Christoffer, A., and Ziese, M.: GPCC Full Data Monthly Product Version 2018 at 1.0°: Monthly Land-Surface Precipitation from Rain-Gauges built on GTS-based and Historical Data, https://doi.org/10.5676/DWD_GPCC/FD_M_V2018_100, 2018b.

Slivinski, L. C., Compo, G. P., Whitaker, J. S., Sardeshmukh, P. D., Giese, B. S., McColl, C., Allan, R., Yin, X., Vose, R., Titchner, H., Kennedy, J., Spencer, L. J., Ashcroft, L., Brönnimann, S., Brunet, M., Camuffo, D., Cornes, R., Cram, T. A., Crouthamel, R., Domínguez-Castro, F., Freeman, J. E., Gergis, J., Hawkins, E., Jones, P. D., Jourdain, S., Kaplan, A., Kubota, H., Blancq, F. L., Lee, T.-C., Lorrey, A., Luterbacher, J., Maugeri, M., Mock, C. J., Moore, G. K., Przybylak, R., Pudmenzky, C., Reason, C., Slonosky, V. C., Smith, C. A., Tinz, B., Trewin, B., Valente, M. A., Wang, X. L., Wilkinson, C., Wood, K., and Wyszyński, P.: Towards a more reliable historical reanalysis:

Improvements for version 3 of the Twentieth Century Reanalysis system, Quarterly Journal of the Royal Meteorological Society, 145, 2876–2908, https://doi.org/10.1002/qj.3598, 2019.

Son, S.-W., Purich, A., Hendon, H. H., Kim, B.-M., and Polvani, L. M.: Improved seasonal forecast using ozone hole variability?, Geophysical Research Letters, 40, 6231–6235, https://doi.org/10.1002/2013GL057731, 2013.

Thiery, W., Davin, E. L., Lawrence, D. M., Hirsch, A. L., Hauser, M., and Seneviratne, S. I.: Present-day irrigation mitigates heat extremes, Journal of Geophysical Research: Atmospheres, 122, 1403–1422, https://doi.org/10.1002/2016JD025740, 2017.

Trewin, B.: A daily homogenized temperature data set for Australia, International Journal of Climatology, 33, 1510–1529, https://doi.org/10.1002/joc.3530, 2013.

van Oldenborgh, G. J., Hendon, H. H., Stockdale, T. N., L'Heureux, M. L., Coughlan de Perez, E., Singh, R. P., and van Aalst, M. K.: Defining El Niño indices in a warming climate, submitted, 2020.

Vautard, R., van Aalst, M. K., Boucher, O., Drouin, A., Haustein, K., Kreienkamp, F., van Oldenborgh, G. J., Otto, F. E. L., Ribes, A., Robin, Y., Schneider, M., Soubeyroux, J.-M., Stott, P. A., Seneviratne, S. I., Vogel, M. M., and Wehner, M. F.: Human contribution to the record-breaking June and July 2019 heat waves in Western Europe, Environ. Res. Lett., 15, 094 077, https://doi.org/10.1088/1748-9326/aba3d4, 2020.

Vose, R. S., Schmoyer, R. L., Steurer, P. M., Peterson, T. C., Heim, R., Karl, T. R., and Eischeid, J. K.: The Global Historical Climatology Network: Long-term monthly temperature, precipitation, sea level pressure, and station pressure data, Tech. Rep. NDP-041, Carbon Dioxide Information Analysis Center, Oak Ridge National Laboratory, Oak Ridge, Tennessee, U.S.A., 1992.

Weisheimer, A., Schaller, N., O'Reilly, C., MacLeod, D. A., and Palmer, T.: Atmospheric seasonal forecasts of the twentieth century: multi-decadal variability in predictive skill of the winter North Atlantic Oscillation (NAO) and their potential value for extreme event attribution, Quarterly Journal of the Royal Meteorological Society, 143, 917–926, https://doi.org/10.1002/qj.2976, 2017.

White, C. J., Hudson, D., and Alves, O.: ENSO, the IOD and the intraseasonal prediction of heat extremes across Australia using POAMA-2, Climate Dynamics, 43, 1791–1810, https://doi.org/10.1007/s00382-013-2007-2, https://doi.org/10.1007/s00382-013-2007-2, 2014.

Williams, A. A. J. and Karoly, D. J.: Extreme fire weather in Australia and the impact of the El Niño-Southern Oscillation, Aust. Met. Mag., 48, 15–22, 1999.

Ziese, M., Becker, A., Finger, P., Meyer-Christoffer, A., Rudolf, B., and Schneider, U.: GPCC First Guess Product at 1.0°: Near Real-Time First Guess monthly Land-Surface Precipitation from Rain-Gauges based on SYNOP Data, https://doi.org/10.5676/DWD_GPCC/FG_M_100, 2011.